IAEA nuclear fusion

PAPER • OPEN ACCESS

Divertor enrichment of recycling impurity species (He, N_2, Ne, Ar, Kr) in ASDEX Upgrade H-modes

To cite this article: A. Kallenbach *et al* 2024 *Nucl. Fusion* **64** 056003

OPEN ACCESS
IOP Publishing | International Atomic Energy Agency
Nuclear Fusion
Nucl. Fusion **64** (2024) 056003 (14pp)
https://doi.org/10.1088/1741-4326/ad3139

Divertor enrichment of recycling impurity species (He, N_2, Ne, Ar, Kr) in ASDEX Upgrade H-modes

A. Kallenbach[1,*], R. Dux[1], S.S. Henderson[2], C. Tantos[3], M. Bernert[1], C. Day[3], R.M. McDermott[1], V. Rohde[1], A. Zito[1] and the ASDEX Upgrade Team[a]

[1] Max Planck Institute for Plasma Physics, D-85748 Garching, Germany
[2] UKAEA, CCFE, Culham Science Centre, Abingdon OX14 3DB, United Kingdom of Great Britain and Northern Ireland
[3] KIT, Karlsruhe, Germany

E-mail: arne.kallenbach@ipp.mpg.de

Received 25 October 2023, revised 26 January 2024
Accepted for publication 7 March 2024
Published 15 March 2024

Abstract

Particle balance calculations are done for the seeding species N_2, Ne, Ar, Kr as well as He with the aim of obtaining a realistic description of the divertor and core plasma impurity content. Experimental time traces of main plasma impurity densities are fitted by a single, time-independent parameter $v_{z,\mathrm{in}}^{\mathrm{eff}}$. This parameter represents the product of the impurity inward pinch in the pedestal, used for the description of gross fueling here, and the enrichment factor between the sub-divertor gas reservoir and the upstream separatrix. $v_{z,\mathrm{in}}^{\mathrm{eff}}$ depends strongly on the first ionization energy as well as on the charge Z or mass of the impurity. The prevailing dependence of the enrichment values on the ionization energy suggests the importance of the relative impurity and deuterium ionization lengths in the divertor. Regression analysis of $v_{z,\mathrm{in}}^{\mathrm{eff}}$ yields an expression for the impurity concentrations in the core and the divertor of ASDEX Upgrade which allows the prediction of the corresponding impurity densities and their divertor enrichment within a factor of 2 with only engineering parameters as input. A simple wall model has been introduced to take into account wall storage and release of impurities, e.g. for conditions of pre-loaded walls due to seeding in previous discharges. Wall effects are observed for all species considered, but wall storage turns out to be more important for N and He compared to Ne, Ar, Kr. Similar enrichment values are obtained for ELMy H-modes and EDA/QCE no-ELM regimes. A factor of approximately 1.4 reduction in enrichment is observed for divertor conditions for pronounced detachment with Ar and N_2. The obtained analytical model for the core and sub-divertor impurity densities is well suited for integration into a discharge flight simulator or a real time state observer.

---

[a] See Zohm *et al* 2024 (https://doi.org/10.1088/1741-4326/ad249d) for the ASDEX Upgrade Team.
[*] Author to whom any correspondence should be addressed.

Keywords: divertor, pumping, impurities, enrichment, ASDEX Upgrade

(Some figures may appear in colour only in the online journal)

1. Introduction

Divertor radiation by seed impurities is required for the necessary spreading of the incident power to a larger divertor surface area and the achievement of partially detached conditions in devices with high power flux like ITER or DEMO [1–3]. Radiation in the outer core is additionally needed for a reduction of the separatrix power flux, P_{sep}, to allow for sufficient divertor dissipation as well as to support MHD activities connected to no-ELM scenarios [4]. The major caveats associated with impurity seeding are the fuel dilution in the core, and a possible degradation of energy confinement due to central radiative losses. Therefore, in particular for the divertor seeding species with its relatively low Z, a high impurity enrichment in the divertor is required [2, 5–7]. In this paper the enrichment is investigated for a number of species and discharge conditions, including a no-ELM scenario. A simple model for impurity concentrations in the main chamber and divertor is developed, aiming at the derivation of robust trends and application in codes requiring fast evaluation like, e.g. a flight simulator.

This paper is organized as follows. We start with a description of the particle balance model in section 2, and the additional model for wall storage and release in section 3. The measurements of the core impurity concentrations for the different species are briefly described in section 4. Comparisons of the balance model with spectroscopic measurements of divertor impurity concentrations are shown in section 5. Section 6 presents a database of obtained enrichment values and the result of its regression analysis. In section 7, a scaling for the parameter $v_{z,\mathrm{in}}^{\mathrm{eff}}$ is derived, which allows the prediction of core impurity densities for stationary deuterium and impurity gas puff rates. Finally, the influence of detachment on the enrichment is discussed in section 8, and conclusions are drawn in section 9.

2. Particle balance model

Although an important quantity, the impurity concentration in the divertor plasma is typically not well determined experimentally and in AUG has only recently become available [8]. Spectroscopic measurements of impurity lines suffer from line-integration of the measured emissivity, uncertainties in atomic data and the limited availability of the plasma parameters (n_e, T_e) required to determine impurity ion densities. The neutral impurity concentration in the neutral gas in the sub-divertor region close to the strike points is more easily accessible. Simple particle balance considerations use particle conservation, namely the equality of puffed and pumped rates for stationary conditions. These lead to an approximate expression for the divertor neutral impurity concentration based on valve flux ratios [9, 10]

$$c_{z,\mathrm{div,valves}} = (\Phi_z/z)\,/\,(\Phi_z/z + \Phi_{\mathrm{D}})\,. \tag{1}$$

Note that valve fluxes Φ are given in ASDEX Upgrade (AUG) in electrons/s and rates refer to atoms, also for molecular species. Equation (1) is expected to be valid for stationary conditions of a saturated wall, i.e. no net particle uptake or release, and equal pumping speeds for deuterium molecules and impurities. Equation (1) has been favourably compared to direct spectroscopic measurements of impurity ion concentrations of N, Ne and Ar [8, 11] as well as to SOLPS modelling [12] in the outer divertor. As will be discussed below, divertor neutral impurity concentrations are effected by variations in neutral conductances and pumping speeds. In the absence of neutral–neutral collisions, conductances scale with the thermal speed of a species. For typical AUG sub-divertor conditions (a drawing can be found in [13]), D_2 molecules are in the intermediate regime between molecular and viscous flow, resulting in an increase of the effective D_2 pumping speed with pressure [14]. Neutral impurities are entrained in the viscous D_2 flow, resulting in an increase of their effective conductances [4]. This effect will be discussed along calculations with the Monte Carlo code DIVGAS [15] described in section 2.1. The impurity entrainment in the D_2 flow can be experimentally tested using the particle removal time, which is dominated by the effective pumping speed. Practically, we use discharges with impurity puffs for different values of the neutral pressure to determine the degree of entrainment.

In order to follow temporal evolutions, and to take advantage of the information entrained in those, a simple time dependent rate equation model is used. Note that ELMy plasma conditions are considered only time-averaged. Simple multi chamber models with empirical communication times have been successfully used in the past for an estimation of divertor compression and enrichment [16–20]. Most important is here to find an ansatz which needs the lowest number of free parameters. An advantage of a time dependent model is that it describes both the steady state impurity content as well as the impurity removal time, allowing to narrow down the free parameters. The model should contain just engineering parameters, or parameters which are available to the control system via real time diagnostics, having also a real time application in mind. Quantities of interest are the impurity divertor compression, defined as ratio of the divertor neutral impurity density and the core ion density, $C_z = \frac{n_{z0,\mathrm{div}}}{n_{z,\mathrm{main}}}$ and the impurity divertor enrichment, $\eta_z = \frac{(n_{z0,\mathrm{div}}\ /\ n_{\mathrm{D0,div}})}{(n_{z,\mathrm{main}}\ /\ n_{e,\mathrm{main}})}$. n_{z0} refers here to neutral sub-divertor densities and n_z to core ion densities. In case of molecular species (D_2, N_2), the divertor densities refer to atoms.

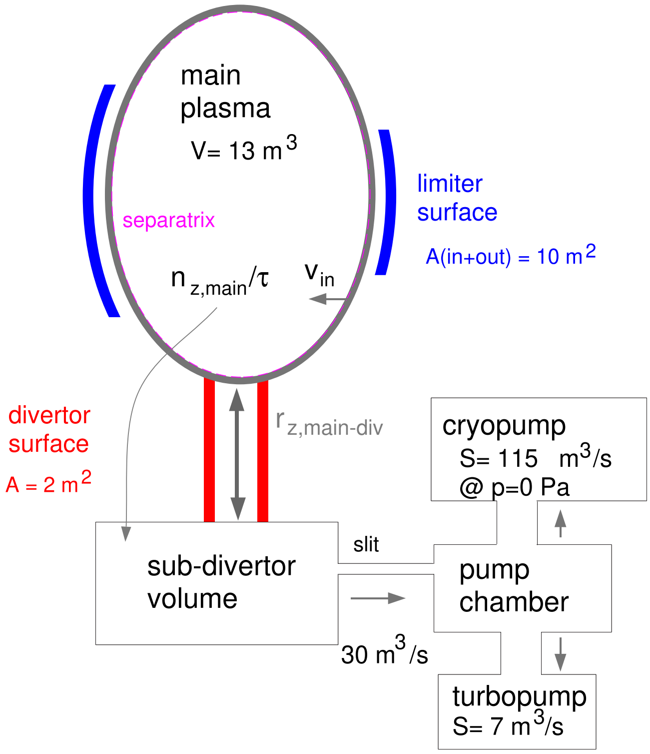

Figure 1. Principle setup of the particle balance model.

We consider 3 volumes as sketched in figure 1, the main plasma volume V_{main}, the sub-divertor volume V_{div} and the pump chamber volume V_{pump}. A corresponding cross section of the real setup can be found in [13]. The main plasma is assumed to contain impurities in partially or fully ionized state only, sub-divertor and pump chamber volumes hold neutral atoms (He, Ne, Ar, Kr) or molecules (N_2). Rate equations are set up for numbers of atoms, while for pumping- and conduction speeds the molecular state is taken into account. For the core impurity density, we obtain

$$\begin{aligned} V_{\text{main}}\, dn_{z,\text{main}}/dt = & -V_{\text{main}}\, n_{z,\text{main}}/\tau_z \\ & + c_{z0,\text{div}}\, n_{e,\text{sep}}\, r_{z,\text{main-div}}\, v_{z,\text{in}}\, A_{\text{sep}} \end{aligned} \tag{2}$$

with $c_{z0,\text{div}} = (n_{z0,\text{div}}/n_{\text{D0}})$ as neutral impurity sub-divertor concentration and $n_{z,\text{sep}} = c_{z0,\text{div}}\, r_{z,\text{main-div}}\, n_{e,\text{sep}}$ as upstream impurity separatrix density. $r_{z,\text{main-div}}$ is the ratio between the impurity concentrations in the midplane and the divertor, which depends on effects of the ionization lengths and impurity-deuteron friction terms [21]. The subscript div stands for the sub-divertor volume. A_{sep} is the plasma surface area at the separatrix. The main plasma impurity confinement time is set fixed to $\tau_z = 0.075 \times I_p/\text{MA}$ [s], corresponding to typical values measured in laser ablation experiments with non-recycling metallic impurities. The current dependence has been introduced following results reported from Alcator C-Mod [22]. A shortening of this time is expected for increasing ELM frequency [23], but we prefer to keep this model as simple as possible. Therefore we neglect all parameter dependencies except that of the plasma current. In reality, the parameter dependencies of τ_z will be more complex. The main plasma source rate (in atoms/s) is expressed by an impurity separatrix density which by convection leads to a particle flux through the plasma surface A_{sep} with an inward pinch velocity $v_{z,\text{in}}$. This flux can be associated with the mainly neoclassical inward flux of impurities through the edge transport barrier, albeit not in absolute value due to the simplified transport model. A potential direct neutral impurity fueling of the core plasma also enters into $v_{z,\text{in}}$. Since we relate the core fueling to the divertor neutral flux ratio, we finally use $v^{\text{eff}}_{z,\text{in}} = r_{z,\text{main-div}} v_{z,\text{in}}$, which is the effective inward convection related to the divertor impurity density. The upstream separatrix electron density $n_{e,\text{sep}}$ is estimated from the neutral divertor pressure via

$$n_{e,\text{sep}} = 2.65\ 10^{19}\ m^{-3}\ p_0^{0.31} \tag{3}$$

with the neutral divertor pressure p_0 in Pascal [13]. This is an empirical relation derived from AUG data, but it can be easily refined and generalized by the 2-point model [10]. p_0 is available in real time from ionization gauge measurements in ASDEX Upgrade, post-pulse additionally from baratrons. For predictive simulations, p_0 can be estimated from a scaling based on the gas puff [24], or by calculating p_0 from the D_2 valve flux using the pumping network as described below. Using the term $c_{z0,\text{div}}\ n_{e,\text{sep}}$ as expression for the upstream impurity density is advantageous comparing to, e.g. using an empirical divertor retention time [25]: as observed for deuterium, also impurities undergo a high compression in the divertor for typical high-power H-mode conditions. This compression is largely reconciled by using p_0 to estimate $n_{e,\text{sep}}$. The sub-divertor volume particle balance reads as following:

$$\begin{aligned} V_{\text{div}} dn_{z0,\text{div}}/dt = & \ \Phi_{z0}/z - (n_{z0,\text{div}} - n_{z0,\text{pumpch}})\ S_{\text{div-pumpch}} \\ & - c_{z0,\text{div}}\ n_{e,\text{sep}}\ r_{z,\text{main-div}}\ v_{z,\text{in}}\ A_{\text{sep}} \\ & + V_{\text{main}} n_{z,\text{main}}/\tau_z \end{aligned} \tag{4}$$

Φ_{z0}/z is the neutral fueling rate, which is supposed to enter in the divertor. Finally, the pumped flux is

$$\begin{aligned} V_{\text{pumpch}} dn_{z0,\text{pumpch}}/dt = & \ (n_{z0,\text{div}} - n_{z0,\text{pumpch}})\ S_{\text{div-pumpch}} \\ & - n_{z0,\text{pumpch}} S_{\text{pump}}. \end{aligned} \tag{5}$$

A complicating effect is the uncertainty in the impurity pumping speed [4]. The pumping network consists of a sub-divertor volume and the pump chamber volume, connected by a slit with a conductivity which is lower compared to the pumping speed of the combined turbo- and cryopumps. The pumping speed for deuterium has been determined from pressure measurements using deuterium puffing into the empty vessel [14]. The D_2 pumping speed rises with pump chamber pressure due to the transition from molecular to viscous flow:

$S_{\text{D2,pump}} = S_{\text{turbo}} + S_{\text{cryo}}$ with $S_{\text{cryo}} = 115\ \text{m}^3\ \text{s}^{-1} + 150\ \text{m}^3/(\text{s Pa}) \cdot p_{\text{D2,pumpch}}$ and $S_{\text{turbo}} = 7\ \text{m s}^{-1}$. For gaseous

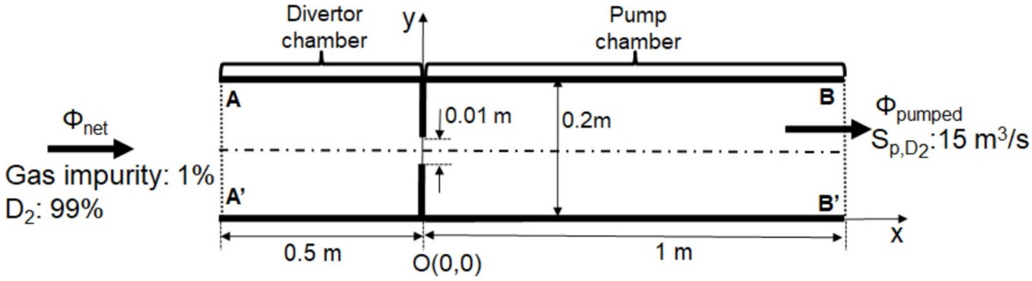

Figure 2. Simplified setup of the pumping network and imposed boundary conditions as used in DIVGAS modelling. The selected volume represents 1 m circumference and thus 1/10 of the sub-divertor region. Therefore the modelled particle throughput and pumping rate represent 1/10 of the experimental values. The slit between sub-divertor volume and pump chamber is aligned in toroidal direction, its width of 1 cm is in line with the actual geometry. A realistic drawing of the experimental geometry can be found in [13].

impurities, the unknown degree of entrainment in the deuterium flow causes uncertainies of the pumping speed. For low pressure conditions, where neutral–neutral collisions can be neglected, pumping speeds and conductances are expected to scale with the thermal speed, or square root of mass ratios. In the other limit of full flow entrainment, equal pumping speeds are expected. For AUG, the conduction through the slit between sub-divertor chamber and pump chamber is most important, since it acts as a bottleneck in the pumping network.

2.1. *Pumping of D_2 and seed impurities*

Deuterium pumping, which exhibits a pressure dependent pumping speed, is known from in-situ calibration [14]. The situation is less clear for seed impurities, since no direct measurements of neutral gas densities in sub-divertor and pump chamber are available and entrainment of impurities in the D_2 flow has to be considered. To shed some light on this, and to obtain a more realistic estimate of the impurity pumping, calculations with the divertor gas simulator (DIVGAS) code [15] were done in a simplified geometry.

The DIVGAS code has been proved to be a reliable tool for the modeling of the neutral gas dynamics in the particle exhaust of tokamaks and stellarators in recent years [15, 26–28]. DIVGAS is a particle-based code, and its main kernel is based on the stochastic direct simulation Monte Carlo (DSMC) method proposed by G. A. Bird in 1963 [29] aiming in solving numerically the Boltzmann equation. The simulated configuration, which is a simplified representation of the real AUG pumping geometry, is shown in figure 2.

In this simplified 2D model, the real AUG divertor-pump chamber geometry is described by a sub-divertor and a pump chamber volume with 10 m circumference (1/10th of which is considered in the calculation) between the sub-divertor region and the pump chamber. These two regions are connected by a gap, which is approximated by a slit of 1 cm width in the calculations. The average heigth of the sub-divertor and pump chamber volumes is set to 0.2 m in the rectangular approximation used. All the solid walls, shown as solid lines in figure 2 are maintained at 300 K. In the modeling a gas mixture, consisting always of 99 % of D_2 and 1% of impurity gas, enters the divertor chamber (left) at 300 K through the inlet line AA' with the net incoming flux varying from 0.05 10^{22} up to 1.2 $\times$ 10^{22} particles/s. Then the gas mixture passing through the slit is expanded into the pumping chamber, where it is pumped at a given pumping speed from the pumping line BB'. In the simulations the pumping process at the pumping line BB', is modelled by applying a capture coefficient ξ for all particles that interact with this boundary line. The particles that hit on the pumping line BB' can be absorbed with a probability ξ, while they can be reflected backwards with a probability 1-ξ. The cryopump in the AUG has a pumping speed for D_2 of around 150 m^3 s^{-1} for medium pressure, and for 1 m chamber in the direction along circumference considered here a pumping speed of 15 m^3 s^{-1} is applied at the pumping line BB', which is equivalent to a capture coefficient of about $\xi = 0.24$ for the deuterium molecules in the case of the absence of intermolecular collisions. This capture coefficient provides the correct pumping speed for a surface area of 0.2 m^2 and an effective speed towards the surface of $\bar{v}/4 = 314$ m s^{-1}, in the low pressure limit. The simulations showed that for $\xi = 0.24$ the presence of the intermolecular collisions slightly increases the actual value of the pumping speed at the pumping surface BB' up to 17 m^3 s^{-1}. Three cases of gas impurities, i.e. Ne, Ar, Kr, have been considered. In all simulations, the cell size in the x- and y-axis was less than 1.7 10^{-3} m and 3.3 10^{-4} m, which ensures that in the regions with sharp gradients the ratio of cell dimension to mean free path is less than 1/3. Also, the time step $\Delta t = 0.1$ μs was chosen sufficiently smaller than the cell traversal time, defined as $\Delta x/u_0$ with u_0 being the most probable speed of the lighter particles (deuterium particles) and Δx is the cell size, to avoid light particles crossing several cells. The average number of the DSMC particles in each simulation ranged from 2 $\times$ 10^8 to 2.5 $\times$ 10^8. To reduce the relative statistical scattering of the macroscopic quantities up to a value significantly smaller than the adopted uncertainty 5 %, the macroscopic quantities were obtained by time averaging over 2 $\times$ 10^6 time-steps after reaching the steady state phase which required about 2 $\times$ 10^6 time-steps. The intermolecular collisions between the particles are modelled according to the reliable no-time-counter (NTC) scheme, supplemented by the variable hard sphere (VHS) model [29]. The viscosity

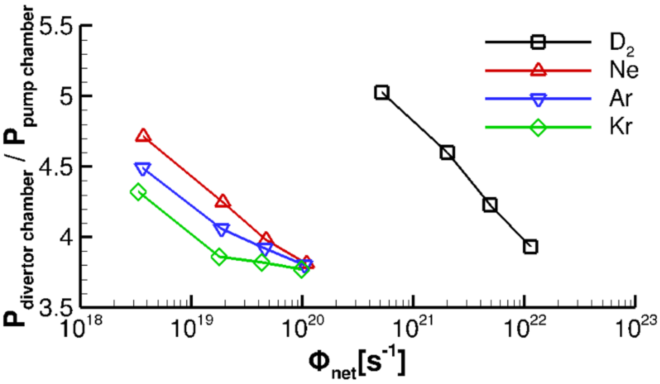

Figure 3. Pressure ratio $P_{\text{divertor chamber}}$/ $P_{\text{pump chamber}}$ vs net flux Φ_{net} of impurities and deuterium.

index parameters of the VHS model for D_2, Ne, Ar, Kr, have been chosen as 0.67, 0.66, 0.81, and 0.8 respectively, with the corresponding reference diameter being 0.292 nm, 0.277 nm, 0.417 nm and 0.476 nm, in order the VHS model to reproduce within 3 % the viscosity experimental data [30, 31] at the reference temperature of 300 K.

Figure 3 shows the variation of the ratio of the average pressure at the divertor chamber to the average pressure at pump chamber with the incoming flux. The incoming flux in this figure represents the partial incoming flux of the deuterium and the noble gases respectively. The pressure of the overall mixture at the divertor chamber was found about 0.81 Pa, 2.73 Pa, 5.75 Pa and 11.9 Pa covering nicely the range of the experimental measurements in AUG. As it is seen in figure 3, for deuterium the pressure ratio $P_{\text{divertor chamber}}/P_{\text{pump chamber}}$ was calculated to be about 4–5, with the corresponding one for impurities being slightly smaller. For this pressure range, the Knudsen number at the divertor chamber and the pump chamber varies as $0.002 < \text{Kn} < 0.04$ and $0.01 < \text{Kn} < 0.2$, respectively. In this regime, the neutral–neutral collisions prevail and cannot be ignored justifying the choice of the DIVGAS code to simulate the entrainment process using this simplified geometric representation. It is also observed that for a given imposed pressure drop, decreasing the atomic mass of the noble gas leads to a higher net flux.

A measure of the intensity of the impurity gas entrainment in D_2 flow is the entrainment factor EF, which can be defined as the ratio of the velocity of the impurities to the velocity of the deuterium, i.e. $\text{EF} = u_{\text{impurity}}/u_{\text{D2}}$. The impurity can be considered to be completely entrained when $\text{EF} = 1$. In figure 4 the distributions of the entrainment factor along the line through the slit at $y = 0.1$ m are shown. The figure shows that for the smallest examined value of the net flux, i.e $\Phi_{\text{net}} = 0.05 \times 10^{22}\ \text{s}^{-1}$, which corresponds also to the more rarefied case compared to the other three higher net flux cases considered here, the entrainment factor remains well below unity in the whole flow domain. Then, as the net flux increases, it is clearly observed that the entrainment factor remains equal to one in most of the flow regions of the divertor and the pump chambers, highlighting the fact that the noble gas particles are fully entrained by the deuterium molecules. It is also observed that as the atomic weight of the particles increases ($m_{\text{Kr}} > m_{\text{Ar}} > m_{\text{Ne}}$), the more difficult it is for the noble gases to be entrained by the deuterium molecules, i.e $\text{EF}_{\text{Kr}} < \text{EF}_{\text{Ar}} < \text{EF}_{\text{Ne}}$. In figure 4 the corresponding distributions of the mole fraction of the noble gases are also presented. As it is expected, in the regions where the noble gases are fully entrained by the deuterium molecules, i.e. $\text{EF} = 1$, the mole fraction of the noble gases remains constant and very close to that imposed at the inlet line AA'. Conversely, in the case where entrainment is weak, i.e. $\Phi_{\text{net}} = 0.05 \times 10^{22}\ \text{s}^{-1}$, the mole fraction variation is more pronounced even in the central regions of both divertor and pump chambers. It is seen that the greater the ratio $m_{\text{impurity}}/m_{\text{D2}}$ the greater the variation in the impurity mole fraction along the flow. This can be explained by the fact that the lighter the noble particles are, the easier it is for them to be entrained by the deuterium ones.

The DIVGAS simulation for deuterium is in line with the expectations by simple engineering formulas. The slit of 1 cm width produces a neutral pressure drop by a factor 4–5 between sub-divertor and pump chamber, as measured in the experiment by baratrons and ionization gauges. For neutral pressures above 1 Pa, the noble gas atoms are fully entrained in the D_2 flow through the slit, a bit reduced entrainment is obtained for a pressure of 0.8 Pa. Close to the pumping surface on the right, the impurity concentration rises, depending on $(m_z/m_{\text{D2}})^{0.5}$ in order to provide sufficient flux to the pump. The capture coefficient of the pump surface has been set equal for D_2 and the noble gas atoms, the density rise is required to compensate the lower thermal speed of the impurities. The local variation of the impurity concentration around the slit is explained by the faster expansion of D_2 behind the slit. The DIVGAS calculations inform the parameter setting of our simplified model. Due to the efficient entrainment of the impurities in the D_2 flow for medium-high p_0, the same conductance through the slit is used for the impurities and D_2, $S_{\text{D2,div-pumpch}} = S_{z,\text{div-pumpch}}$. For the lowest pressure conditions, this leads to a modest overestimation of the pumping speed. $S_{\text{div-pumpch}}$ is chosen to match the pressure drop between sub-divertor and pump chamber, which comes close to the conductance of the 1 cm slit in the simplified geometry model. In real geometry, the slit has a minimum width of about 1.5 cm, but is extended along the x-direction in figure 2. It should be noted that small effects of by-passes between the chambers and the main chamber are omitted here. The impurity cryo pumping speed is scaled with the inverse square-root-of-mass ratio.

2.2. Time-independent expressions for core and divertor concentrations

In order to develop an analytical description which describes quasi-stationary conditions, we derive in the following the time-independent solution of the equations of section 2. The

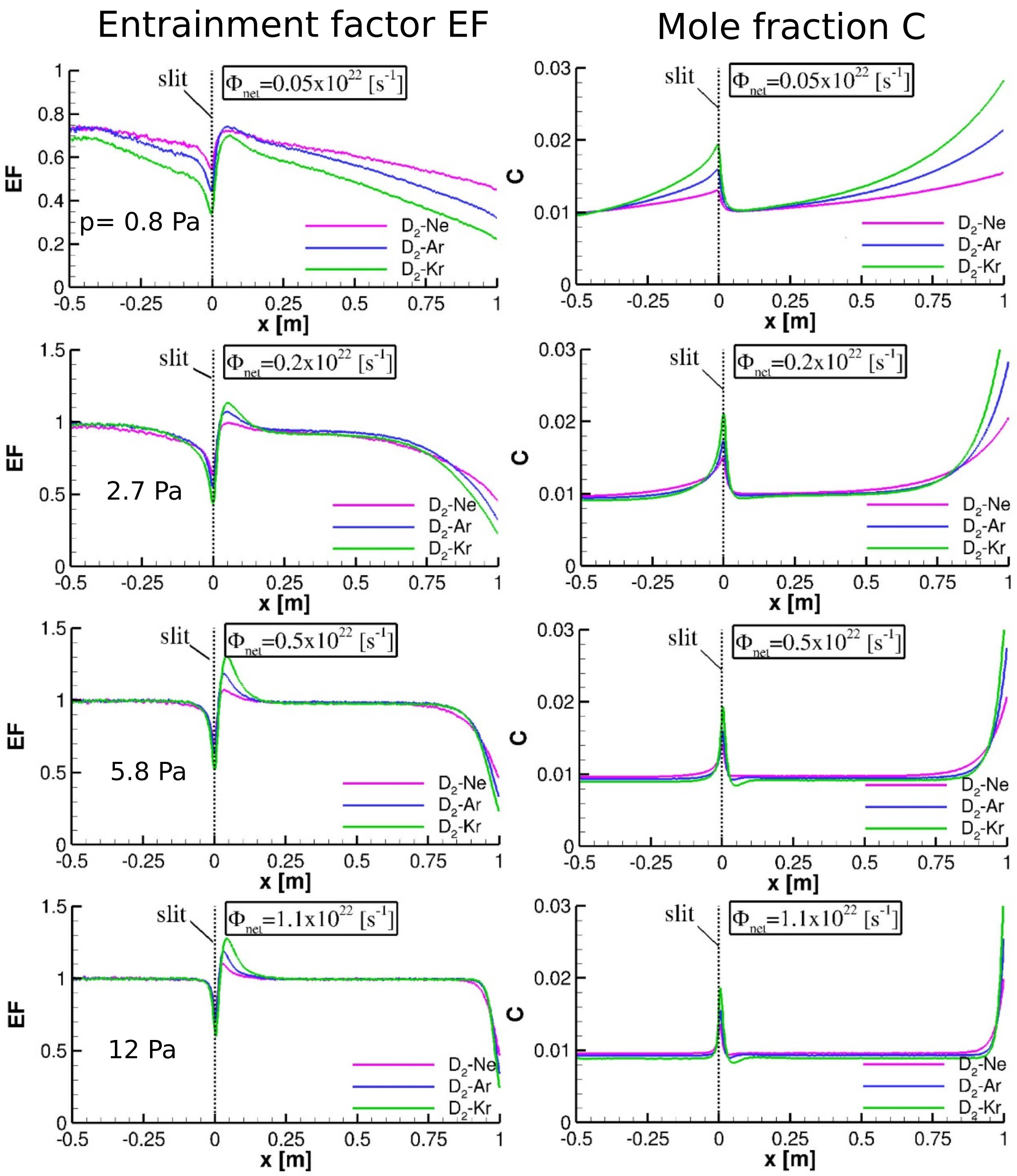

Figure 4. Distributions of the entrainment factor $\mathrm{EF} = \mathrm{u}_{\mathrm{impurity}}/\mathrm{u}_{\mathrm{D2}}$ (left) and impurity mole fraction $c = n_{\mathrm{impurity}}/(n_{\mathrm{D2}} + n_{\mathrm{impurity}})$ (right) along the line $y = 0.1$ m (see the dash-dotted line in 2.1) for various net fluxes Φ_{net} and for the three examined impurity cases.

sub-divertor pressure is related to the pump chamber pressure and the pumping speed via the stationary gas throughput balance:

$$n_{z0,\mathrm{pumpch}} = (\Phi_{z0}/z)/S_{z,\mathrm{pump}} = n_{z0,\mathrm{div}} \frac{S_{z,\mathrm{div-pumpch}}}{S_{z,\mathrm{pump}} + S_{z,\mathrm{div-pumpch}}}. \tag{6}$$

The deuterons in the sub-divertor region are assumed to be at room temperature and in molecular state, $n_{\mathrm{D0}} = f_{np} \cdot p_0$ with $f_{np} = 4.84 \times 10^{20}$ at/(m^3 Pa). We obtain an explicit formula for the divertor neutral impurity concentration:

$$c_{z0,\mathrm{div}} = \Phi_{z0}/\left(z f_{np}\, p_0\right) \times \frac{S_{z0,\mathrm{pump}} + S_{z0,\mathrm{div-pumpch}}}{S_{z0,\mathrm{div-pumpch}} S_{z0,\mathrm{pump}}}. \tag{7}$$

The particle balance model can also be applied to D$_2$ gas puffing for conditions of negligible wall storage/release, allowing to express p_0 by the deuterium gas puff and using equation (6) for D$_2$. We obtain

$$\begin{aligned} c_{z0,\mathrm{div}} &= \phi_{z0}/z\phi_{\mathrm{D}} \times \\ \frac{S_{z0,\mathrm{pump}} + S_{z0,\mathrm{div-pumpch}}}{S_{z0,\mathrm{div-pumpch}} S_{z0,\mathrm{pump}}} &\times \frac{S_{D2,\mathrm{div-pumpch}} S_{D2,\mathrm{pump}}}{S_{\mathrm{D2,pump}} + S_{\mathrm{D2,div-pumpch}}}. \end{aligned} \tag{8}$$

The contribution of the impurity to the total neutral pressure has been omitted here for clarity. We immediately see, that equation (8) reproduces the simple gas valve flux ratio equation (1) for conditions of equal pumping speeds and conductances for neutral impurities and D$_2$ molecules, where the factor in the second row of equation (8) turns 1.

The DIVGAS calculations suggest to use $S_{z,\mathrm{div-pumpch}} = S_{\mathrm{D2,div-pumpch}}$ due to the high entrainment of the impurities in the D$_2$ flow from divertor to pump chamber. From figure 4 we see that for low pressures, the entrainment reduces to a value of

0.8. This leads to a slight (up to 20 %) underestimation of the divertor concentration in our database for low values of p_0 due to the overstimation of $S_{z,\mathrm{div-pumpch}}$. For the pumping speed of the cryopump, we assume the standard square root of mass ratio $(\frac{m_{\mathrm{D2}}}{m_{z0}})^{0.5}$ of the pumping speeds. Due to the much lower pressure in the pump chamber compared to the sub-divertor region (≈factor 5), we assume approximately molecular flow conditions in the pump. In the simplified DIVGAS modelling figure 4, we see a rise of the impurity concentration at the pumping surface roughly by the mass ratio $(\frac{m_{z0}}{m_{\mathrm{D2}}})^{0.5}$ (deviation of 10–40 %), which is required to sustain the pumped flux with the pumping speeds scaling with the inverse $(\frac{m_{\mathrm{D2}}}{m_{zo}})^{0.5}$ factor. The moderate increase of the deuterium pumping speed with pressure found in in-situ measurements of the pumping speed, caused by molecular deuterium collisions, is likewise adpated to the impurity pumping, accounting for a moderate entrainment in the pump flow. With our assumptions on conductances and pumping speed, the de-enrichment factors factor given by the 2nd line of equation (8), which increase the divertor neutral impurity concentration due to their weaker pumping, turn (1.2, 1.25, 1.33, 1.55) for (Ne, N_2, Ar, Kr) for a neutral pressure of 2 Pa. The (partial) entrainment into the particle flow through the conductance between sub-divertor and pump chamber reduces the predicted impurity concentration in the sub-divertor region. Finally, we obtain the expression for the core impurity density. Assuming stationary conditions, core—separatrix balance reveals

$$V_{\mathrm{main}} n_{z,\mathrm{main}}/\tau_z = c_{z,\mathrm{main}} \overline{n}_{e,\mathrm{main}} V_{\mathrm{main}}/\tau_z = v^{\mathrm{eff}}_{z,\mathrm{in}} A_{\mathrm{sep}} c_{z0,\mathrm{div}} n_{e,\mathrm{sep}}. \tag{9}$$

The main plasma volume for AUG is 13 m^3 and the separatrix surface area $\mathrm{A}_{\mathrm{sep}} = 43\ \mathrm{m}^2$ for typical equilibria. For the core plasma density, we obtain the following prediction:

$$n_{z,\mathrm{main}} = \tau_z v^{\mathrm{eff}}_{z,\mathrm{in}} A_{\mathrm{sep}} c_{z0,\mathrm{div}} n_{e,\mathrm{sep}}/V_{\mathrm{main}}. \tag{10}$$

A scaling for the parameter $v^{\mathrm{eff}}_{z,\mathrm{in}}$ will be presented in section 7. Inserting equation (1) or (7) for $c_{z,\mathrm{div}}$, approximate predictions for impurity content, compression and enrichment are obtained, based on engineering parameters and an analytic scaling for $v^{\mathrm{eff}}_{z,\mathrm{in}}$ only.

3. Model additions for wall storage and release

For modeling of time dependent, non-stationary conditions, the effect of wall surfaces on the particle balance has to be taken into account. The storage and release of particles at the wall is caused by the incoming particle flux and the sputtering by impurities and fuel ions. Due to the different areas and time constants, main chamber and divertor wall elements are considered separately. The incoming flux densities $\Gamma_{z,w}$ are related to the deuterium neutral pressure and corresponding impurity concentrations. The local fluxes are in terms of ions or neutrals, depending on local conditions. Since the neutral deuterium flux measured in the main chamber by ionisation gauges is mainly caused by ion fluxes towards the wall, both quantities are expected to exhibit a similar behaviour. Nevertheless, the assumptions made bare significant uncertainties. The neutral deuterium flux corresponds to the neutral flux density at the given neutral pressure, times the divertor surface area. The impurity flux is assumed to be $c_{z0,div}$ times the thermal speed ratio times the deuterium flux. For the main chamber limiters, flux densities are assumed to be a factor 50 lower compared to the sub-divertor. This factor has been chosen at the lower limit of typical neutral flux density ratios between 50 and 300 in ASDEX Upgrade [32], since the limiters see higher flux densities compared to the locations of the neutral main chamber gauges. The impurity fluxes to limiter and divertor surfaces lead to wall storage, while impurity and fuel fluxes release impurities stored in the wall.

The change of the number of impurity atoms $N_{z,w}$ at a wall element with surface area A_w and saturation surface area density $n_{z,w,\mathrm{sat}}$ is described by

$$\begin{aligned} dN_{z,w}/dt = {} & A_w\ (\Gamma_{z,w}\ (1-r)\ (1-N_{z,w}/(A_w\ n_{z,w,\mathrm{sat}})). \\ & -\ Y\Gamma_{\mathrm{D}}\ N_{z,w}/\left(A_w\ n_{z,w,\mathrm{sat}}\right) \end{aligned} \tag{11}$$

Stored and realeased particles are assumed to be exchanged with the neutral particle reservoir in the sub-divertor. Ideal surface areas of 2 m^2 for the divertor and 10 m^2 for the limiters are assumed, representing the regions which are mostly exposed to the plasma and neutral fluxes. r is the particle reflection coefficient for the impinging impurities. The release yield Y, for fully saturated surfaces, is related to the impinging D flux at main chamber and divertor walls, assuming a fixed impurity mix resulting in a release yield by the impact of deuterons and impurity ions. The actual yield Y_{eff} is assumed to scale with the wall saturation fraction, $Y_{\mathrm{eff}} = \mathrm{Y}\ \frac{N_z/A_W}{n_{z,w,\mathrm{sat}}}$, with the Y values given in table 1. For the case of helium, the corresponding atomic and surface science data have been discussed in [33], for the other impurities discussed in this Paper, the corresponding parameters were matched to fit the experimental data.

Nitrogen storage under laboratory conditions in polished *W* surfaces was measured by [35]. Saturation was observed there around 50% atomic N content in the near surface layer, and saturation densities of $1.1 \times 10^{20}\ \mathrm{m}^{-2}$ for 500 eV and $2.3 \times 10^{20}\ \mathrm{m}^{-2}$ for 2500 eV impact energy. The moderately higher values used for N in this work may be attributed to the technical surface conditions. The nitrogen impact energy on the AUG divertor surface is expected to be below 100 eV for typical divertor temperatures. Another factor with influence on the saturation density as well a the removal is the effect of recoil collisions, which compete with sputtering collisions. A recoil collision leads to a deeper penetration of the N in the W bulk [35]. The effects of ammonia formation [36, 37] are not taken into account in our simple wall model. Atomistic simulations of Ne implantation in tungsten were performed by [38]. Much lower Ne implantation was found compared to He, as well as a saturation of Ne storage at a fluence of several 10^{20} Ne atoms per m^2.

Table 1. Surface model parameters for main chamber and divertor walls. Particle reflection coefficients are taken from [34], evaluated for 50 eV impact energy and 30^0 impact angle from ⊥. For Kr, where no data are given in [34], a dedicated calculation with SDtrimSP was used. Indicated saturation density values were derived assuming effective divertor areas $A_{\mathrm{div}} = 2$ m^2 and $A_{\mathrm{main}} = 10$ m^2. Kr data are put in brackets due to higher uncertainties of individual parameters.

Element	Helium	Nitrogen	Neon	Argon	Krypton
reflection r	0.72	0.69	0.7	0.66	0.4
saturation density [at/m^2]	2×10^{20}	1×10^{21}	5×10^{18}	5×10^{18}	(2×10^{18})
Y	2.5×10^{-2}	3×10^{-2}	2×10^{-3}	2×10^{-3}	(2×10^{-4})

The parameters shown in table 1 were determined by matching the time dependence of short impurity puffs as well as the steady state conditions during discharges with long (several s) impurity injection times. While the combination of the surface model parameters saturation density, sputtering yield Y, surface areas and flux ratios yield a good desription of the time dependent impurities in AUG within the simple model, the found combination does not have to be unique. E.g. lower surface areas in combination with higher flux and saturation densities may give identical results. Also, surface roughness effects may affect saturation densities and sputtering.

Other uncertainties enter from the use of collective fluxes (neutrals plus ions) without consideration of the energy distribution to divertor and wall for storage and release, and possible changes of the background impurity content. To shed some light on the influence of the wall model, figure 5 shows also the effect of a variation of the surface areas by factor 2 and 1/2. The factor varies the assumed main chamber and divertor wall areas (2 and 10 m^2, respectively). Due to the higher impinging flux densities and its lower surface area, the divertor is more important for changes on short time scales, while the main chamber walls are less active, but more important on long time scales. For low neutral pressure, the divertor surface approaches steady state in a time scale of ≈0.1 s for Ne and Ar, while the main wall changes over seconds and dominates the latency in between plasma discharges. At higher p_0, the time scales shorten with increasing flux densities. Figure 5 shows also core neon densities for a high neutral pressure comparison case. The higher neutral divertor compression results in a factor 4 lower impurity density (normalized on identical gas puff amplitude) and a much faster removal time. Note also that both shots are well modelled with similar values of $v_{z,\mathrm{in}}^{\mathrm{eff}}$, in line with the regression analysis results. The lower core neon density and its faster decay at high p_0 are caused by the higher neon divertor compression, which follows p_0 and thus the higher deuterium compression in our modelling ansatz. The neon particle balance for the two conditions of figure 5 is shown in figure 6 both assuming no neon wall pre-load and a pre-load of 0.1 × the assumed saturation fraction. With higher neutral pressure much faster pumping occurs, and the wall time scales shorten correspondingly. Shortly after closure of the gas valve, the majority of particles outside the pump reside in the plasma and the main chamber wall. For high neutral pressure, most of the particles are pumped. Also a neon release from the preloaded wall is observed. The effect of the wall loading on the core plasma content remains relatively small for neon.

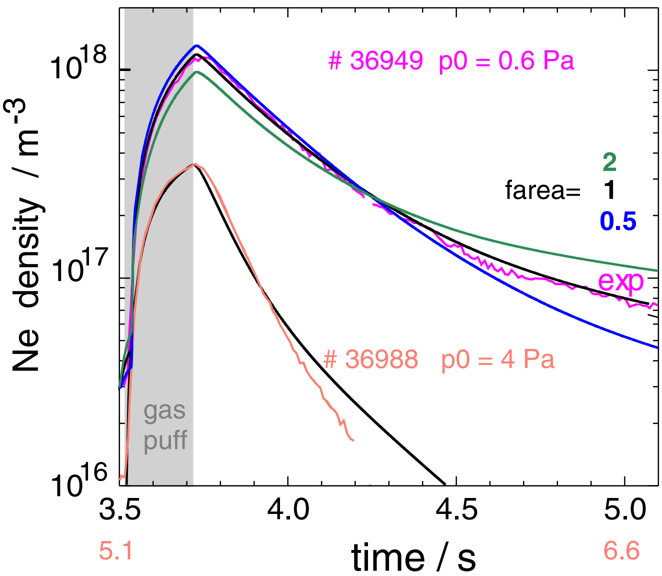

Figure 5. Time traces of the neon density for low neutral divertor pressure in the core plasma from CXRS spectroscopy (magenta) and balance modelling (36949, $v_{z,\mathrm{in}}^{\mathrm{eff}} = 19$ m s^{-1}). A variation of the main chamber and divertor surface areas by factors 0.5 and 2 is shown to demonstrate the wall storage effect. brown/black: measured and modelled (36988, $v_{z,\mathrm{in}}^{\mathrm{eff}} = 14$ m s^{-1}) time trace for high neutral pressure and standard areas. To show the pure effect of the different p_0 values, the measured and modelled neon densities for # 36988 have been multplied by 2.3 since the gas puff rate was lower by this factor compared to # 36949 (puff duration about 0.2 s each and rates 8.5 10^{19} atoms/s for # 36988 and 1.9 10^{20} atoms/s for # 36949). The global 1/e decay time for Ne halves from 0.3 to about 0.15 s from low to high neutral pressure p_0. All other transport parameters kept constant, standard pumping with cryo and turbopumps. $P_{\mathrm{heat}} = 7.5$ MW, $I_p = 0.8$ MA. Time traces of a similar shot of the same series can be found in figure 11 of [4].

4. Determination of core impurity concentrations for particle balance calculations

Impurity densities for He, N, Ne and Ar are obtained from CXRS measurements [39]. For He, N and Ne fully stripped species are measured, while for Ar the helium-like stage Ar^{16+} is used, which dominates in the outer part of the core plasma [40]. The uncertainty of the CXRS rate coefficients is with ± 20% largest for argon. Since full profiles of argon are not available, the measurement of the Ar^{16+} around around its radial maximum at $\rho_{\mathrm{pol}} = 0.75{-}0.85$ is taken, multiplied by the factor 1.2 to account for the contributions of Ar^{15+} and Ar^{17+}

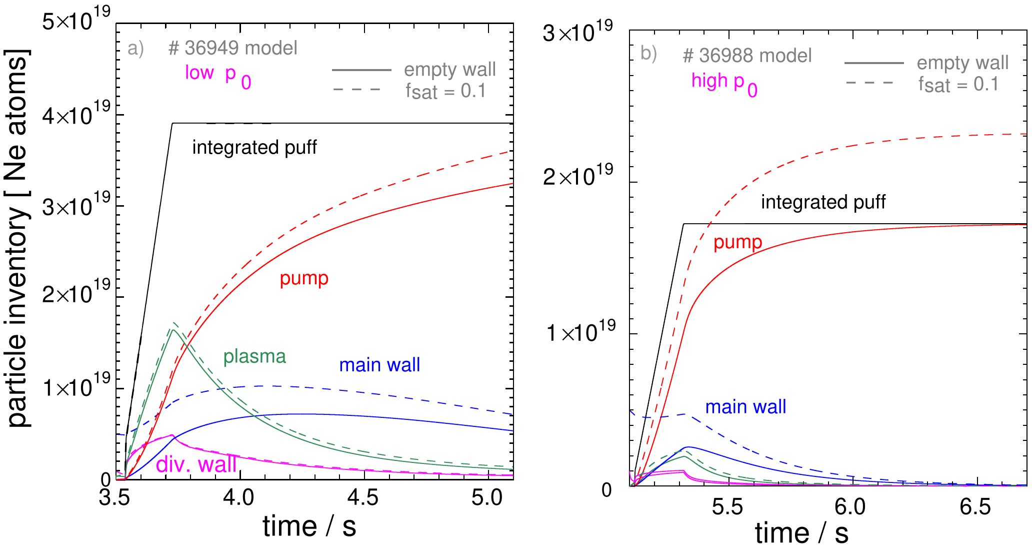

Figure 6. Calculated particle balance for the Ne puff cases of figure 5 and standard areas for no wall pre-loading (solid lines) with Ne and a Ne pre-loading of 0.1 × the saturation fraction (dahed lines). (*a*) low $p_0 = 0.6$ Pa, # 36949. (*b*) high $p_0 = 4$ Pa, # 36988. The actual experimental situation corresponds to 0.1 × the saturation fraction pre-loading for # 36949 in (*a*) due to previous Ne seeded discharges and no wall pre-loading in (*b*).

to the total argon density. Helium-like Ar is dominant in the outer core plasma due to the large factor (≈4.5) between the ionization potentials of Ar^{15+} and Ar^{16+}. The core concentration is then determined by division by the line-averaged density measured by interferometry [41, 42]. The same procedure is used for N^{7+} and Ne^{10+}, without a correction factor for the ion abundance since both elements are fully stripped under the experimental conditions considered. In the case of He, correction for plume effects have been applied in the course of the CXRS evaluation [43]. For Krypton, no CXRS measurements are available. Instead, measurements by soft-X ray cameras, a VUV spectrometer and bolometry have been combined in an analysis with the impurity transport code STRAHL to obtain Kr concentrations, following a procedure described in [44]. The core concentrations used in this study represent the gross values, relevant for the particle balance. Potential impurity density profile peaking effects are neglected, since core transport effects are reduced into the single global impurity confinement time τ_z.

5. Test of the model for nitrogen and argon seeding

For a discharge with combined nitrogen and argon seeding, direct spectroscopic measurements of the divertor impurity ion concentrations were obtained by the method of Henderson [8, 11, 45] and compared to the simple estimate equation 1 and the prediction of the time dependent particle balance model, see figure 7. Modelled core densities have been fitted via the time-independent parameter $v^{\mathrm{eff}}_{z,\mathrm{in}}$ (1.65 m s^{-1} for N and 4.2 m s^{-1} for Ar), divertor densities are a consequence of particle balance in the model.

After a few seconds of seeding, when the walls are in equilibrium, quite good agreement between the simple gas puff ratio and the direct spectroscopic measurements is obtained. The neutral concentrations of the balance model are higher than the simple formula 1. One has to keep in mind, that the spectroscopic measurements give the ion concentration in the divertor plasma, which is different from the neutral concentration in the sub-divertor. The good agreement of the ionic concentrations with the simple formula 1 reported in [11] may be interpreted that the ionic plasma concentration is more closely related to the ratio of the neutral fluxes rather than the neutral densities. Indeed, close agreement with the spectroscopic ion concentrations is obtained when neutral concentrations are expressed in terms of flux ratios instead of density ratios, see grey curves in figures 7(b) and (c). A direct proof of the mass dependent effective pumping speed by comparisons to spectroscopic ion density measurements appears not possible. Given the combined uncertainties, krypton should be used due to its large mass ratio to D_2, but spectroscopic divertor ion density measurements are not yet available for this element.

6. Enrichment database

A database has been set up combining the particle balance analyses from deuterium H-mode discharges seeded with N_2, Ne, Ar, Kr and He for further comparisons. The particle balance model described in section 3 was used to track the measured time dependent impurity concentration $c_{z,\mathrm{main}}$, with $v^{\mathrm{eff}}_{z,\mathrm{in}}$ as the only fitting parameter which is also assumed constant in time. Data base entries were derived from shorter phases of these discharges (typically several 100 ms) with constant values of

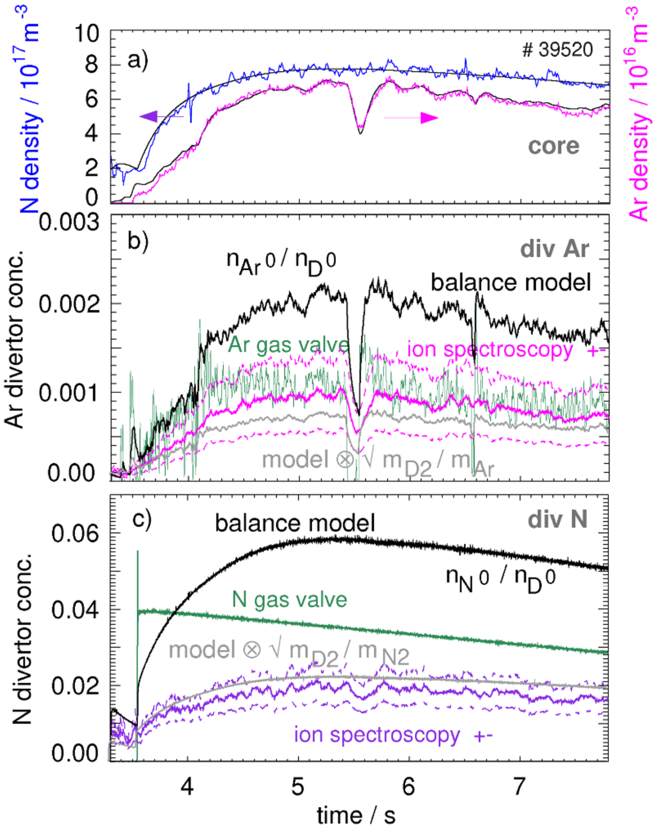

Figure 7. Time traces of measured core densities and divertor impurity ion concentrations [11] of Ar (magenta) and N (blue) in a discharge with feedback on power entering the divertor (Ar) and a feed-forward N puff. Black lines show the balance modelling results. (*a*) core densities of N and Ar and the balance model fit (black). Measured Ar^{16+} concentrations were multiplied by the factor 1.2 for extrapolation to full Ar densities. (*b*) measured divertor argon impurity ion concentration with upper and lower uncertainty (magenta), the result of the balance model (black) and the simple gas valve ratio equation (1) (green). (*c*) as (*b*) for nitrogen. The grey lines are the divertor concentrations in terms of flux ratios, the neutral density ratio times the square root of mass ratio. $I_p = 1$ MA, $p_0 \approx 2$ Pa, $P_{\mathrm{heat}} = 12$ MW. D puff of 3.4 10^{22} atoms/s.

the deuterium and impurity puffs and quasi-stationary impurity densities. For discharges with short impurity puffs, which are particulary valuable for testing the exhaust model, enrichment values were derived by extrapolation in time until stationary conditions were achieved keeping plasma parameters and $\nu_{z,\mathrm{in}}^{\mathrm{eff}}$ frozen.

The data base contains 45 entries from 33 discharges with a plasma current of 0.7–1 MA and a heating power of 7.5–17 MW. 8 data base entries are from no-ELM scenarios EDA/QCE H-mode [46]. 5 data base entries refer to helium in ELMy H-mode. He data are only shown as a test for the model, they were not included in the regression analysis due to the higher uncertainties produced by the strong wall storage. Except for 4 data point entries, which will be discussed in section 8, the database consists of attached or partially detached plasma conditions in the outer divertor. The inner divertor is detached in all discharges. The impurity concentration in the divertor, $c_{z,\mathrm{div}}$, is provided via particle conservation by the particle balance model. The major error for this parameter results from uncertainties in the conductance between sub-divertor and pumping chamber and pumping speed, depending on the entrainment.

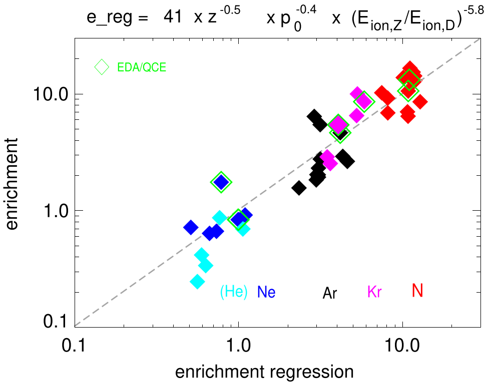

Figure 8. Regression result of the impurity divertor enrichment η_z versus impurity charge Z, divertor neutral pressure p_0 and ionisation energy $E_{\mathrm{ion},z}$. Green framing indicates discharges in no-ELM EDA or QCE regime. He data have not been included in the fit, their regression values are based on the fit result obtained from N, Ne, Ar and Kr.

The derived enrichment values were investigated by a regression analysis. First, the most important experimental parameters were identified which determine the enrichment, afterwards a multi-parameter regression analysis with these parameters was performed. The most important parameter is the neutral ionisation energy, $E_{\mathrm{ion},z}$, followed by the atomic charge Z, which leads to almost identical regression results when exchanged by the mass m_z, and finally the divertor neutral pressure, p_0. Figure 8 shows the regression result versus the experimental enrichment values derived via the balance model. Figure 9 displays the contribution of the individual regression parameters. The dominance of the neutral ionisation energy is interpreted as the effect of the neutral impurity ionisation depth in comparison to deuterium. The divertor impurity enrichment reduces with increasing neutral pressure $p_0^{-0.4}$. A higher Z or mass leads to reduced enrichment, opposite to the trend expected from penetration depth decreasing with decreasing thermal speed, suggesting the predominance of neoclassical effects in the pedestal. Regression of the impurity compression gives a similar dependence on charge and ionisation energy as obtained for the enrichment, but a rise with neutral pressure $\propto p_0^{0.5}$.

7. Empirical scalings for the core impurity density and divertor enrichment

Expressing the separatrix density via the neutral pressure, the formulas derived in section 2 allow the prediction of the core impurity density with one free parameter only, namely $\nu_{z,\mathrm{in}}^{\mathrm{eff}}$.

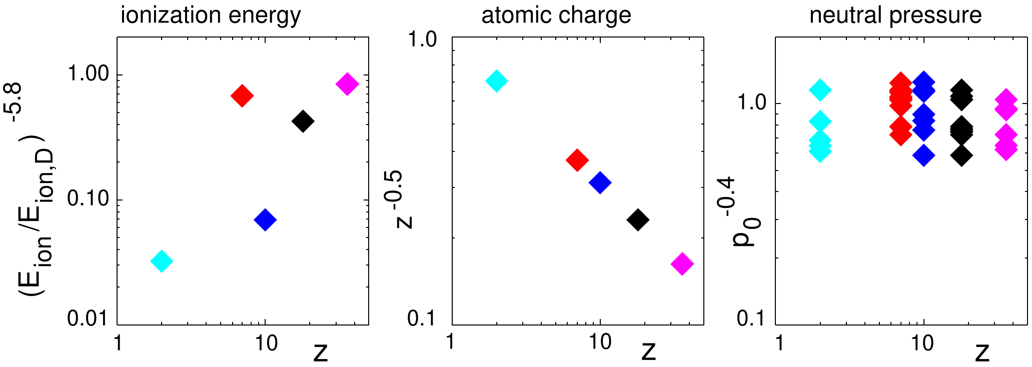

Figure 9. Contribution of the individual regression parameters to the power law enrichment model shown in figure 8. Dominant are the neutral ionization energy and the charge Z.

Table 2. First ionization potentials and masses for the exhaust species, taken from physics.nist.gov. The average charge $<Z>$ was calculated for $T_e = 300$ eV assuming Corona equilibrium. The last line shows the parameter $v^{eff}_{z,in}$, see figure 10(*a*). He was not included in the fit due to the strong impact of wall processes, the $v^{\mathrm{eff}}_{z,\mathrm{in}}$ given in brackets is the extrapolation from the seeding gas fits based on ionization energy and mass.

Species	D	D_2	He	N	N_2	Ne	Ar	Kr
Z	1		2	7		10	18	36
$<Z>$ @ $T = 500$ eV	1.0		2.0	7.0		9.7	15.7	20.3
ionization energy / eV	13.6	15.47	24.59	14.53	15.58	21.56	15.76	14.00
mass / amu	2.01	4.03	4.00	14.0	28.01	20.2	39.95	83.8
$v^{eff}_{z,in}$ / m s^{-1}			(13.5)	1.3		17.3	3.85	3

A regression analysis was done for $v^{\mathrm{eff}}_{z,\mathrm{in}}$, using only atomic parameters, with the result shown in figure 10(*a*). Helium data were not included in the regression since they are too strongly influenced by wall storage and release, but the resulting $v^{\mathrm{eff}}_{z,\mathrm{in}}$ fit also describes the helium content quite well.

The strongest parameter dependence is found for the neutral ionization energy of the impurity species. This is clearly related to the ionization length, whose relation to the ionization length of deuterons was identified as a strong player for divertor retention in SOLPS modelling [12, 21, 47, 48]. The dependence on the (full) charge Z can be related to collisional processes. A probable candidate is neoclassical transport in the pedestal region, which leads to a stronger influx of higher Z impurities due to the fact that the neoclassical $v_{z,\mathrm{in}}/D$ scales with Z [49–52]. Calculations with the FACIT routine [53] for pedestal parameters yield an about linear dependence of the neoclassical inward drift from the charge Z when toroidal plasma rotation is not taken into account. With typical pedestal top rotation values, centrifugal effects increase the inward drift for the heavier elements Ar and Kr, leading to a stronger than linear Z dependence. A contribution of collisional process in the divertor may not be ruled out, but here the local ionisation stage should be considered. The effect of ELMs may have weakened the observed Z dependence compared to the pure neoclassical expectation. Since there is a single $v^{\mathrm{eff}}_{z,\mathrm{in}}$ for each species, remaining dependencies on plasma parameters show up as vertical spread in figure 10, which also contains the errors of the divertor impurity concentration derived from the simple gas puff ratios.

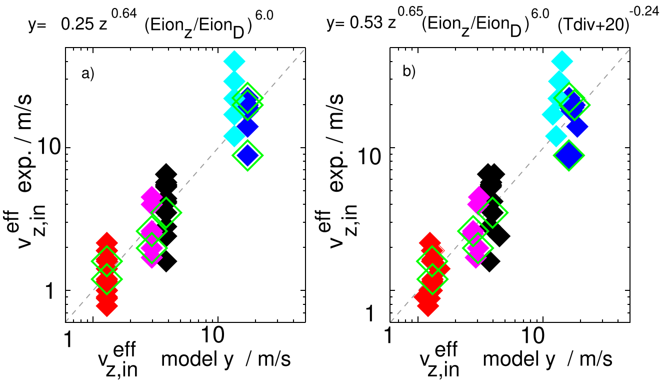

Figure 10. Regression fit for the parameter $v^{\mathrm{eff}}_{z,\mathrm{in}}$ used for the prediction of the core impurity density. (*a*) Just using atomic parameters Z, E_{ion}. (*b*) Including Tdiv into the regression, see section 8. Knowledge of Tdiv reduces the rmse from 42 to 39%.

With the scaling obtained,

$$v^{\mathrm{eff}}_{z,\mathrm{in}} = 0.25\ Z^{0.64}\left(E_{\mathrm{ion},z}/E_{\mathrm{ion,D}}\right)^{6.0}\ [m/s] \tag{12}$$

see also table 2, the core impurity density can be predicted with atomic and engineering parameters only. We use the valve fluxes for calculating the divertor impurity concentration according to equation (8). The neutral divertor pressure p_0 is derived from the gas valve fluxes using equation (6) applied for deuterium, but could also for higher accuracy be taken

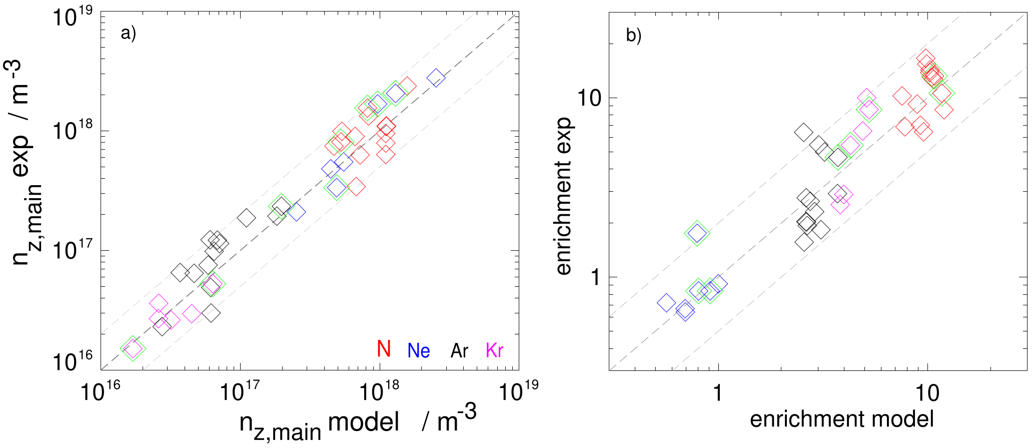

Figure 11. (*a*) Measured main plasma impurity densities versus prediction using the fit for $\nu_{\mathrm{in},z}^{\mathrm{eff}}$ shown in figure 10(*a*) and equations (7) and (10). (*b*) Measured and predicted enrichment values. Only engineering parameters / gas valve fluxes are used for the prediction of $n_{z,\mathrm{main}}$. The dotted lines mark deviations of prediction and measurement by a factor 2. For 15 database entries from transient impurity puffs, the measured densities/enrichment values have been extrapolated to stationary conditions.

from real time measurements or an empirical fit formula taking more parameters into account [24]. For the prediction of the core impurity density, the neutral pressure p_0 enters only via $n_{e,\mathrm{sep}} \propto p_0^{0.31}$, which causes a very small impact of the error of ± 25% induced by the estimation of p_0 via the valve fluxes. Wall storage and release effects are neglected for the predictive calculations. Figure 11(*a*) compares the prediction of the main plasma impurity density to the measured values of the seed impurities. Core impurity densities are matched within a factor of 2 (mean relative error of 36%), with the main parameter $\nu_{z,\mathrm{in}}^{\mathrm{eff}}$ depending on atomic data only. The no ELM EDA/QCE discharges included in the database do not significantly deviate, suggesting similar impurity transport. Figure 11(*b*) compares the predicted enrichment values with the measured ones. The measured line-averaged density has been used here to evaluate the core impurity concentration. Again a match within about a factor of 2 is obtained, using gas valve fluxes with equations (8), (10) and the regression fit figure 10(a) for $\nu_{z,\mathrm{in}}^{\mathrm{eff}}$. The prediction for the plasma impurity content can be further improved by the inclusion of plasma parameters in the fit for $\nu_{z,\mathrm{in}}^{\mathrm{eff}}$. One element is plasma detachment, which causes an increased seed impurity content and hence increased $\nu_{z,\mathrm{in}}^{\mathrm{eff}}$, and is discussed in the following.

8. Influence of divertor detachment

If the divertor approaches deep detachment, one expects a reduction in neutral plugging due to a reduction of the electron temperature, and hence a reduction of divertor enrichment [19]. This has been tested by exchanging the neutral pressure p_0 by the divertor temperature Tdiv, obtained from shunt measurements [54], in the regression shown in figure 8. Tdiv roughly equals T_e measured by Langmuir probes in the outer divertor SOL close to the strike points, but may turn zero or negative during pronounced detachment [2] since the outer divertor is no longer the wall contact with the highest T_e. In the present dataset, Tdiv varies between −7 and 21 eV. To avoid log of negative numbers connected to pronounced detachment, Tdiv +20 has been used instead for regression. An increase in enrichment as $(\mathrm{Tdiv}{+}20)^{0.29}$ is obtained. Adding Tdiv+20 into the regression analysis for $\nu_{z,\mathrm{in}}^{\mathrm{eff}}$ yields a dependence $\nu_{z,\mathrm{in}}^{\mathrm{eff}} \propto (\mathrm{Tdiv}{+}20)^{-0.24}$, see figure 10(*b*).

To shed further light on the impact of detachment, a dedicated discharge was analysed where the heating power was modulated to switch between attached and detached conditions, combined with nitrogen and argon seeding [11]. Figure 12 shows experimental time traces and balance modelling of this discharge. The change in impurity transport is quite well described by a stepwise switch of $\nu_{z,\mathrm{in}}^{\mathrm{eff}}$ between attached and detached phases. The switching is triggered by NBI heating steps, which change the power to the divertor since the main chamber radiation changes less than the heating power. The total radiated power varies less, since during the detached phase, an X-point radiator [55] develops, which leads to a redistribution of the radiation, but does not contribute to Pradmain as evaluated. The time development of the impurity content is very well captured, in view of the quite simple transport model. The divertor enrichment of N reduces during detachment by the factor ≈1.5 for nitrogen and ≈1.4 for argon. $\nu_{z,\mathrm{in}}^{\mathrm{eff}}$ changes inversely by similar factors. This is in qualitative agreement with results from Ar seeding in Alcator C-Mod, where the reduced divertor enrichment was related to a larger ionization mean free path.

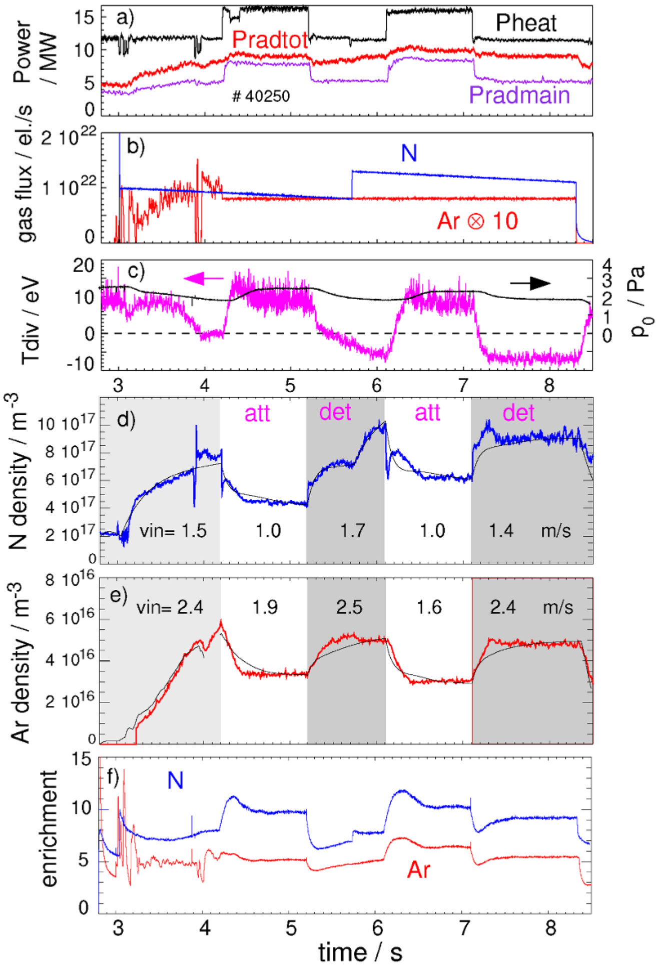

Figure 12. Plasma parameters and balance modelling of a discharge with attached and detached phases, achieved by heating power variations and N and Ar seeding. (*a*) heating power and total and main chamber radiated power. (*b*) Ar and N gas valve fluxes [el./s]. (*c*) Tdiv (magenta) and neutral divertor pressure p_0 (black). (*d*) N core density from balance model (solid black) and CXRS measurement (blue). (*e*) modelled core Ar density (black) and CXRS measurement ($Ar^{16+} \times 1.2$) (red). (*f*) divertor enrichment (flux related) for N and Ar from balance model. $I_p = 1$ MA, $q_{95} = 4.4$.

9. Conclusions

An impurity particle balance model has been developed which allows the evaluation of divertor enrichment and the prediction of core impurity densities for H-mode conditions in ASDEX Upgrade. The model is fast and needs only engineering parameters as input, making it suitable for flight simulator or real time applications. For slow enough variation of the gas puff rates (compared to τ_z) and stationary wall loading, the model allows the prediction of the core and divertor impurity densities within a factor of 2. The dominating parameter for divertor impurity enrichment is found to be the neutral ionization energy of the impurity atom. In line with previous modelling work (e.g. [48]) and combined experimental and modelling studies at DIII-D [56, 57], a short ionization mean free path, caused by a low first ionization potential, results in a high divertor enrichment. A higher charge Z leads to a weak opposite effect, presumably either due to collisional effects in the divertor or due to enhanced neoclassical inward transport in the pedestal. With the divertor impurity concentration mainly determined by particle balance, the core density can be well described by the single parameter $v_{z,\mathrm{in}}^{\mathrm{eff}} = 0.25$ $(E_{\mathrm{ion},z}/E_{\mathrm{ion,D}})^{6.0} Z^{0.64}$ (m s^{-1}). $v_{z,\mathrm{in}}^{\mathrm{eff}}$ can be interpreted as the product $v_{z,\mathrm{in}}\, r_{z,\mathrm{main-div}}$, where $v_{z,\mathrm{in}}$ describes the inward transport at the pedestal and $r_{z,\mathrm{main-div}}$ the impurity concentration ratio between midplane (ions) and divertor (neutrals). Effects of divertor compression are built into the model by the relation of upstream separatrix density and divertor neutral pressure, $n_{e,\mathrm{sep}} =\ 2.65\ 10^{19}\ m^{-3}\ p_0^{0.31}$ [13], which also reproduces the increasing impurity compression with rising neutral pressure. The only plasma physics assumption embedded into the model is the global impurity confinement time τ_z, with the simple dependence on plasma current $\tau_z = 0.075$ (I_p /MA) [s]. Further refinements are possible, e.g. by inclusion of the divertor temperature into $v_{z,\mathrm{in}}^{\mathrm{eff}}$, but not required at the aspired level of precision in this simple approach. No significant differences in impurity behaviour was found for no-ELM scenarios EDA/QCE H-mode compared to standard ELMy H-mode cases, suggesting that the impurity transport in the pedestal caused by the MHD activity which prevents the ELMs is not very different from the transport caused by ELMs.

Despite significant simplifications in the description of the pumping network and the particle transport, robust trends could be demonstrated for the wall sticking and enrichment behaviour of the seeding impurities N, Ne and Ar. N wall storage is of high importance for the N particle balance. Lower storage of the order of a mono-layer is also observed for Ne, Ar and Kr, but still important for the particle balance. The helium recycling pattern is even dominated by storage and release by tungsten wall. As found in modelling with the DIVGAS neutral particle code in a simplified pumping geometry, the seeding gases are fully entrained in the D_2 flow from sub-divertor into the pump chamber except for the lowest neutral pressures. This speeds up their removal rate and is an important element in the reproduction of the global impurity decay times.

Generally, impurity compression rises with the fuel compression, albeit slower compared to deuterium, resulting in moderately decreasing enrichment with increasing p_0. Divertor detachment leads to a moderate reduction of the enrichment by the factor 1.4–1.5 for N and Ar. This effect has been found to be more pronounced with helium [33]. The very low divertor enrichment observed for neon and helium is attributed to the high ionization energy of its neutral, leading to deeper penetration into the divertor plasma compared to the deuterons. Such an effect is not predicted by SOLPS-ITER modelling for ITER divertor conditions [21]. More modelling studies will be required, which on the one hand reproduce the experimental situation in ASDEX Upgrade, and on the other hand apply the validated model with full physics to ITER geometry.

Acknowledgments

We thank Daniel Fajardo for calculating neoclassical pinch values with the FACIT routine. This work has been carried out within the framework of the EUROfusion Consortium, funded by the European Union via the Euratom Research and Training Programme (Grant Agreement No 101052200 - EUROfusion). Views and opinions expressed are however those of the author(s) only and do not necessarily reflect those of the European Union or the European Commission. Neither the European Union nor the European Commission can be held responsible for them.

ORCID iDs

A. Kallenbach https://orcid.org/0000-0003-0538-2493
S.S. Henderson https://orcid.org/0000-0002-8886-1256
C. Tantos https://orcid.org/0000-0003-1382-2364
R.M. McDermott https://orcid.org/0000-0002-8958-8714
A. Zito https://orcid.org/0000-0002-6743-6568

References

[1] Pitts R. *et al* 2019 *Nucl. Mater. Energy* **20** 100696
[2] Kallenbach A. *et al* 2013 *Plasma Phys. Control. Fusion* **55** 124041
[3] Subba F., Coster D.P., Moscheni M. and Siccinio M. 2021 *Nucl. Fusion* **61** 106013
[4] Kallenbach A. *et al* 2021 *Nucl. Fusion* **61** 016002
[5] Kallenbach A. *et al* 2015 *Nucl. Fusion* **55** 053026
[6] Siccinio M., Federici G., Kembleton R., Lux H., Maviglia F. and Morris J. 2019 *Nucl. Fusion* **59** 106026
[7] Asakura N. *et al* 2021 *Nucl. Fusion* **61** 126057
[8] Henderson S.S. *et al* 2018 *Nucl. Fusion* **58** 016047
[9] Kallenbach A. *et al* 2017 *Nucl. Fusion* **57** 102015
[10] Kallenbach A., Bernert M., Dux R., Eich T., Henderson S.S., Pütterich T., Reimold F., Rohde V. and Sun H.J. 2019 *Nucl. Mater. Energy* **18** 166
[11] Henderson S. *et al* 2023 *Nucl. Fusion* **63** 086024
[12] Hitzler F., Wischmeier M., Reimold F. and Coster D.P. 2020 *Plasma Phys. Control. Fusion* **62** 085013
[13] Kallenbach A. , Sun H.J., Eich T., Carralero D., Hobirk J., Scarabosio A. and Siccinio M. 2018 *Plasma Phys. Control. Fusion* **60** 045006
[14] Rohde V. , Mertens V. and Scarabosio A. 2009 *J. Nucl. Mater.* **390–391** 474
[15] Varoutis S. , Tantos C. and Day C. 2021 *Plasma Phys. Control. Fusion* **63** 104001
[16] Roth J. , Krieger K. and Fussmann G. 1992 *Nucl. Fusion* **32** 1835
[17] Kallenbach A. *et al* 1995 *Nucl. Fusion* **35** 1231
[18] Dux R. *et al* 1996 *Plasma Phys. Control. Fusion* **38** 989–99
[19] Goetz J., Lipschultz B., Pitcher C.S., Terry J.L., Bonoli P.T., Rice J.E. and Wukitch S.J. 1999 *J. Nucl. Mater* **266–269** 354
[20] Wade M. *et al* 1999 *J. Nucl. Mater* **266–269** 44
[21] Sytova E. *et al* 2019 *Nucl. Mater. Energy* **19** 72
[22] Rice J.E. *et al* 2015 *Nucl. Fusion* **55** 033014
[23] Dux R. 2003 *Fusion Sci. Technol.* **44** 708
[24] Luda T., Angioni C., Dunne M.G., Fable E., Kallenbach A., Bonanomi N., Schneider P.A., Siccinio M. and Tardini G. 2020 *Nucl. Fusion* **60** 036023
[25] Dux R. , Janzer A. and Pütterich T. 2011 *Nucl. Fusion* **51** 053002
[26] Bonelli F., Varoutis S., Coster D., Day C. and Zanino R. 2017 *Nucl. Fusion* **57** 066037
[27] Tantos C., Varoutis S. and Day C. 2020 *J. Vac. Sci. Technol.* B **38** 064201
[28] Tantos C., Varoutis S., Day C., Balbinot L., Innocente P. and Maviglia F. 2022 *Nucl. Fusion* **62** 026038
[29] Bird G. 1994 *Molecular Gas Dynamics and the Direct Simulation of Gas Flows* (Oxford University Press)
[30] Hirschfelder J. *et al* 1964 *Molecular Theory of Gases and Liquids* 2nd edn (Wiley)
[31] Kestin J., Knierim K., Mason E.A., Najafi B., Ro S.T. and Waldman M. 1984 *J. Phys. Chem. Ref. Data* **13** 229
[32] Kallenbach A. *et al* 2003 *Nucl. Fusion* **43** 573
[33] Zito A. *et al* 2023 *Nucl. Fusion* **63** 096027
[34] Eckstein W. 2002 Calculated sputtering, reflection and range values *Technical Report* 9/132 (IPP) (available at: https://pure.mpg.de/rest/items/item_2138250/component/file_2138249/content)
[35] Meisel G. *et al* 2014 *New J. Phys.* **16** 093018
[36] Neuwirth D., Rohde V. and Schwarz-Selinger T. 2012 *Plasma Phys. Control. Fusion* **54** 085008
[37] Drenik A. *et al* 2019 *Nucl. Fusion* **59** 046010
[38] Backman M., Hammond K.D., Sefta F. and Wirth B.D. 2016 *Nucl. Fusion* **56** 046008
[39] McDermott R.M. *et al* 2018 *Plasma Phys. Control. Fusion* **60** 095007
[40] McDermott R., Dux R., Guzman F., Pütterich T., Fischer R. and Kappatou A. 2021 *Nucl. Fusion* **61** 016019
[41] Mlynek A. , Schramm G., Eixenberger H., Sips G., McCormick K., Zilker M., Behler K. and Eheberg J. 2010 *Rev. Sci. Instrum.* **81** 033507
[42] Mlynek A. , Casali L., Ford O. and Eixenberger H. 2014 *Rev. Sci. Instrum.* **85** 11D408
[43] Kappatou A. , McDermott R.M., Pütterich T., Dux R., Geiger B., Jaspers R.J.E., Donné A.J.H., Viezzer E. and Cavedon M. 2018 *Plasma Phys. Control. Fusion* **60** 055006
[44] Dux R. , Cavedon M., Kallenbach A., McDermott R.M., Vogel G. and ASDEX Upgrade team T. 2020 *Nucl. Fusion* **60** 126039
[45] Henderson S.S. *et al* 2021 *Nucl. Mater. Energy* **28** 101000
[46] Faitsch M. *et al* 2023 *Nucl. Fusion* **63** 076013
[47] Reimold F., Wischmeier M., Potzel S., Guimarais L., Reiter D., Bernert M., Dunne M. and Lunt T. 2017 *Nucl. Mater. Energy* **12** 193
[48] Senichenkov I.Y., Kaveeva E.G., Sytova E.A., Rozhansky V.A., Voskoboynikov S.P., Veselova I.Y., Coster D.P., Bonnin X. and Reimold F. 2019 *Plasma Phys. Control. Fusion* **61** 045013
[49] Dux R. , Peeters A.G., Gude A., Kallenbach A., Neu R. and Team A.U. 1999 *Nucl. Fusion* **39** 1509
[50] Dux R. and Peeters A.G. 2000 *Nucl. Fusion* **40** 1721
[51] Pütterich T. , Dux R., Janzer M.A. and McDermott R.M. 2011 *J. Nucl. Mater.* **415** S334
[52] Casali L., Fable E., Dux R. and Ryter F. 2018 *Phys. Plasmas* **25** 032506
[53] Fajardo D., Angioni C., Maget P. and Manas P. 2022 *Plasma Phys. Control. Fusion* **64** 055017
[54] Kallenbach A. *et al* 2010 *Plasma Phys. Control. Fusion* **52** 055002
[55] Bernert M. *et al* 2020 *Nucl. Fusion* **61** 024001
[56] Casali L. *et al* 2020 *Phys. Plasmas* **27** 062506
[57] Casali L., Eldon D., McLean A., Osborne T., Leonard A., Grierson B. and Ren J. 2022 *Nucl. Fusion* **62** 026021